Astron. Astrophys. 338, 340–352 (1998)

ASTRONOMY AND ASTROPHYSICS

Asteroids as far-infrared photometric standards for ISOPHOT⋆

T.G. Müller[1,3] **and J.S.V. Lagerros**[2]

[1] Max-Planck-Institut für Astronomie, Königstuhl 17, D-69117 Heidelberg, Germany
[2] Astronomiska observatoriet, Box 515, S-75120 Uppsala, Sweden
[3] ISO Science Operations Centre, Astrophysics Division, Space Science Department of ESA, Villafranca, P.O. Box 50727, E-28080 Madrid, Spain

Received 11 February 1998 / Accepted 22 June 1998

Abstract. Asteroids are used as far-IR calibrators for the imaging photopolarimeter ISOPHOT on board the Infrared Space Observatory ISO. For the 10 selected objects we compiled a large uniform database[1] of 678 individual observations, ranging from 7–2 000 μm.

Applying a new thermophysical model to the observations we derived thermal properties of the selected asteroids, based on spin-vector solutions, direct size measurements and the HG-magnitude system.

Our investigations indicate very rough surfaces, reflected in the beaming effect, and very low levels of heat conduction, expressed in thermal inertias between 5 and 25 $\mathrm{J\,m^{-2}\,s^{-0.5}\,K^{-1}}$. Due to scattering processes in the porous regolith, the emissivity varies significantly with wavelength. In case of Vesta we find emissivities as low as 0.6 in the far-IR / submillimetre region.

By entering the combined results into the thermophysical model we defined new photometric standards for the far-IR. The absolute accuracy for thermal flux or lightcurve predictions is 5–10 % for the first category objects and 10–20 % for the secondaries. The methods and procedures discussed here are included in the first update of the ISOPHOT calibration in 1998.

Key words: minor planets, asteroids – radiation mechanisms: thermal – infrared: solar system

1. Introduction

With the successful launch of the *Infrared Space Observatory* (ISO) (Kessler et al. 1996) in November 1995 it has been necessary to establish a set of celestial standards for the photometric calibration of the instruments. In collaboration between the PIDT[2] and external experts a sample of 10 asteroids had been selected (C. Telesco, D. Osip, priv. communication) in support of the imaging photopolarimeter ISOPHOT (Lemke et al. 1996) They show only small lightcurve variations over typical observational integration times of less than 30 minutes, although their absolute lightcurve amplitudes of up to 30 % have to be known for our purposes. Their excellent visibility during the mission and the absence of strong emission or absorption features supported this decision. From the technical aspect of filter leak effects the asteroids have the advantage of low fluxes at short wavelengths (compared to stellar SEDs). The selected objects cover the flux range between 1 Jy (brightest standard stars) and 1 000 Jy (Uranus and Neptune) at wavelengths between 50 and 200 μm (Fig. 1). Even if the majority of point sources observed with ISOPHOT are fainter, the calibration of the detector system must be established for a wide variety of sky surface brightness levels. There are many regions in the sky where the background alone contributes more than several Jy per diffraction limited beam, which is about 42″ for ISO at 100 μm. Due to this strong thermal emission of interplanetary and interstellar dust, the asteroids provide an important brightness level in the far-IR, although most of interesting sources are much fainter.

Most of the selected objects are well observed, but the requested high flux accuracy of better than 10 % made it necessary to conduct additional investigations. From 1995 to 1997 we obtained targeted ground-based mid-IR and submillimetre / millimetre observations, as well as special ISOPHOT calibration measurements. Additionally we re-analysed published IRTF[3], JCMT[4], HHT[5] and IRAS[6] data to convert the published inband fluxes to individual monochromatic flux densities. This process resulted in a large database for the 10 asteroids. The uniformity of the database entries allows us to select subsamples by object, wavelength region, time period, instrument or data quality for extensive comparisons with different model predictions and parameter settings.

It was clear from the beginning that the requested high accuracy can only be achieved by a full treatment of the thermal behaviour and the modelling or monitoring of the lightcurve

Send offprint requests to: T.G. Müller, (tmueller@mpia-hd.mpg.de)

⋆ The ISOPHOT data are based on observations with ISO, an ESA project with instruments funded by ESA Member States (especially the PI countries: France, Germany, the Netherlands and the United Kingdom) and with the participation of ISAS and NASA.

[1] Table 7 is only available in electronic form at the CDS via anonymous ftp to cdsarc.u-strasbg.fr (130.79.128.5) or via http://cdsweb.u-strasbg.fr/Abstract.html

[2] ISOPHOT Instrument Dedicated Team

[3] Infrared Telescope Facility

[4] James Clerk Maxwell Telescope

[5] Heinrich-Hertz-Telescope

[6] Infrared Astronomical Satellite

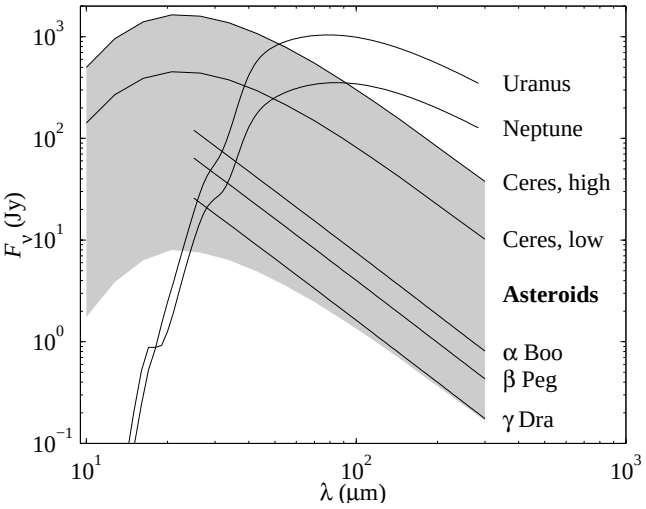

Fig. 1. The brightness levels of celestial standards used for the ISOPHOT far-IR calibration. The shaded area indicates the approximative range covered by the selected asteroids, during the ISO-mission. The predictable flux variations of the asteroid, due to rotation, are in the order of 5–30 % on timescales of several hours. The changing earth–asteroid distance can cause an absolute flux in-/decrease of one order of magnitude on a yearly timescale, as is exemplified by the indicated flux range of Ceres. Uranus and Neptune cover the upper dynamic range of the ISOPHOT long-wavelengths detectors (calculated for Oct., 16 1996, M. Abbas, priv. communications, based on Lindal 1992). The extrapolation of the stellar spectra are described in Cohen et al. (1996). The brightest standard stars have fluxes below $1\,\mathrm{Jy}$ at far-IR wavelength (data products have been provided by M. Cohen, 1996, for the ISO calibration).

variations due to the rotation of the non-spherical objects. A first approach to evaluate the relevance of thermal properties was the application of the Standard Thermal Model (STM) (Lebofsky & Spencer 1989, and references therein) to the observations. The STM is a well tested and popular model, used extensively for the interpretation of IRAS and ground-based broadband mid-IR photometry. It has also been used for the relative calibration of the IRAS $100\,\mu\mathrm{m}$-band against the $60\,\mu\mathrm{m}$-band (Beichmann et al. 1988). In the STM the asteroids are considered to be spherical, with surfaces of negligible thermal inertias. Two empirical correction parameters, the beaming parameter η and the phase angle correction β, are used in order to obtain good agreement with observations. In spite of this simplicity it has proven to be successful, but for the calibrational requirements of ISOPHOT the STM has some shortcomings. The spherical asteroid shapes fail to predict any light curve variations, and the physical meaning of the correction parameters is somewhat unclear, especially when extending the model from the mid- to the far-IR. This can be seen for example in the analysis of the IRAS photomety, where the derived radiometric diameters vary systematically from 12 to 25, 60 and $100\,\mu\mathrm{m}$ (Spencer et al. 1989). In principle it is possible to handle these and other issues by adding more adjustment parameters to the STM and applying light curve corrections. This, however, violates the simplicity argument as well as introduces more empirical factors of unknown physical origin.

A new thermophysical model (TPM) has been developed throughout a series of papers by Lagerros (1996, 1997, 1998). The shape and spin state of the asteroids are taken into account. The physical processes within the surface are handled by including heat conduction, surface roughness, and scattering in the regolith. In comparison to the STM the new model is an attempt towards more physical understanding of the processes behind the thermal emission of asteroids.

We apply the TPM to our database of observations and derive the important thermophysical quantities. The methods used are described in Sect. 5. We demonstrate their functioning and in Sect. 6 we discuss the reliability of the results. We achive our goal of excellent agreement with observational data at all thermal wavelength by using the TPM with individual input parameters for each asteroid. In Sect. 7 we summarize the implications and give a short outlook.

2. The thermophysical model

The thermophysical model of asteroids used here has been discussed in detail by Lagerros (1996, 1997, 1998). In essence, the surface temperature is calculated from the energy balance between absorbed solar radiation, the thermal emission, and heat conduction into the surface material. The disk integrated model flux at the wavelength λ is

$$F_\lambda = \frac{1}{\pi\Delta^2} \oint_S \varepsilon_\mathrm{d} B_\lambda(\gamma T) \mu \, dS, \tag{1}$$

where Δ is the distance to the observer, B_λ the Planck function, and the direction cosine μ projects the surface element dS towards the observer. The "beaming function" γ, and the wavelength- and direction-dependent emissivity ε_d are discussed below.

The most important aspects of the model parameters are outlined in the following:

2.1. Shape, size and spin vector

An estimate of the size and shape of the asteroid is required for the surface integral in Eq. (1). Essentially any shape can be used in the model, from perfectly spherical to highly irregular. In this case (except for 4 Vesta as discussed below) the shapes are assumed to be ellipsoids. For the shape and spin vector the following input parameters are used by the model:

$2a$	major ellipsoid axis $[\mathrm{km}]$
$a/b, b/c$	ellipsoid axis ratios
P_sid	rotational period $[\mathrm{days}]$
$\lambda_\mathrm{p}, \beta_\mathrm{p}$	ecliptic longitude and latitude of spin vector $[^\circ]$
γ_0	absolute rotational phase at the time JD_0

For asteroids of the sizes and rotational periods considered here, the damping time scale for tumbling asteroids to principal-axis rotation is short, compared to the collision time scale (Burns &

Safronov 1973). Thus, the spin vector is assumed to be given in a right-handed system and parallel to the semi-minor axis c.

The absolute size is a key physical property, since from Eq. (1) the disk integrated flux is proportional to the projected area ($F_\lambda \propto a^2$) at all wavelengths.

In order to predict the flux at any given time it is necessary to know the orientation and position of the asteroid relative to the Sun and the observer. The positional data is given from celestial mechanics at a very high precision.

The orientation can be computed for any time if the spin vector and the absolute rotational phase at an epoch JD_0 are known. Together with the axis ratios it is possible to predict the projected area of the ellipsoid at any given time, and hence the light curve.

2.2. Albedo and emissivity

The temperature at a given point on the surface is determined by several factors. The albedo gives the fraction of reflected solar radiation, while the remaining fraction is absorbed and heats the surface. The cooling is determined by the wavelength dependent hemispherical emissivity. The model parameters are:

G	slope parameter
p_V	geometric albedo
$\varepsilon_{\rm h}(\lambda)$	the hemispherical emissivity

where G is the slope parameter for the phase curve in the HG-magnitude system (Bowell et al. 1989). Together with the geometric albedo this gives the Bond albedo, which is assumed to be close to the bolometric albedo.

The emissivity is used for two purposes. First, the hemispherical emissivity averaged over wavelength (weighted by the Planck function) gives the "bolometric emissivity". Secondly, the $\varepsilon_{\rm h}(\lambda)$ is tied to the volume single scattering albedo of the regolith particles. By this it is possible to derive the directional emissivity $\varepsilon_{\rm d}$ used in Eq. (1).

2.3. Heat conduction

Heat conduction has the effect of lowering the amplitude of the diurnal temperature variations. In general, by increasing the thermal conductivity, more energy is emitted on the night side at the expense of the day side temperature. There is also a morning / afternoon asymmetry in the flux due to the thermal inertia. The model parameter for the heat conduction is

Γ	thermal inertia [$\mathrm{J\,m^{-2}\,s^{-0.5}\,K^{-1}}$]

where $\Gamma = \sqrt{\kappa_{\rm s}\rho_{\rm s}c_{\rm s}}$, with $\kappa_{\rm s}$ being the thermal conductivity, $\rho_{\rm s}$ the density and $c_{\rm s}$ the heat capacity of the surface material.

The heat conduction is much more important at the shorter IR wavelengths. The importance for the far-IR calibration is that mid-IR ground-based photometry is used, for which the thermal inertia have to be taken into account.

2.4. The thermal IR beaming

The thermal emission from atmosphere less solar system bodies like the Moon or the asteroids has a tendency to be "beamed" into the solar direction. This behaviour is probably due to the large surface roughness and porosity. The beaming function γ corrects the temperature for this effect in Eq. (1). The beaming function is calculated by adding spherical segment craters (Lagerros 1998) to a smooth surface. The roughness is described by the model parameters

f	fraction of surface covered by craters
ρ	r.m.s. of the surface slopes

The beaming is a very noticeable effect, and can be studied by investigating the non-Lambertian phase curves of asteroids.

2.5. Multiple scattering

Many asteroids are probably rather irregular, which means that there can be multiple scattering and mutual heating between well separated parts of the surface. Multiple scattering can be taken into account (Lagerros 1997) by adding a term for the scattered field to Eq. (1). This option is not used here, since in general it makes only a minor effect, and the shapes of the asteroids are not known well enough to model it in detail.

3. Properties of the individual asteroids

An overview of the model parameters is provided in Table 1. The shape, the spin-vector and the HG values are the essential input parameters for the thermophysical modelling. The shape is generally described as an ellipsoidal with the axis ratios a/b and b/c. Only for 4 Vesta a more sophisticated shape model, based on HST results (Thomas et al. 1997), could be used. The rotation periods vary from a few hours to more than one day. The spin-vector can not always be derived unambiguously from lightcurve observations (Magnusson et al. 1989). The limited observational coverage for 10 Hygiea, 54 Alexandra, 65 Cybele and 313 Chaldaea leads to an ambiguous solution (A. Erikson, priv. communication, 1997). Müller (1997) investigated the effects of both spin-vector solutions on the basis of ratios between observations and predicted fluxes. The parameters which produced the lowest scatter in the ratios were considered as the more realistic solution.

We use the IAU two-parameter magnitude system for asteroids (Bowell et al. 1989), termed also as the HG-magnitude system. H is the *absolute magnitude*, G is the *slope parameter*. Both values are used to derive radiometric diameters and albedos from observational data.

1 Ceres The H and G have been determined from several apparitions, with good coverage at small phase angles (Lagerkvist et al. 1992). The weighted mean of H from available apparitions is used here. The size and shape of Ceres have been determined from occultation observations combined with previous diameter measures and extensive photoelectric photometry (Millis et

al. 1987). There exists also a lower accuracy shape model based on speckle observations (Schertl et al. 1995), which is not used here. Considering the very low amplitude of the Ceres lightcurve (Tedesco et al. 1983), less than $0.04\,\mathrm{mag}$, it is quite difficult to extract a pole position by the classical method of lightcurve inversion. We use a prograde spin vector, perpendicular to the ecliptic ($\lambda_\mathrm{p} = 0°$, $\beta_\mathrm{p} = 90°$). This is in good agreement with the conclusions of Millis et al. (1987), Spencer et al. (1989) and also with the considerations of Saint-Pe et al. (1993). Merline et. al. (1996) found indications for surface albedo variations on Ceres from HST imaging. They are not taken into account in the following.

2 Pallas The H and G values are taken from Lagerkvist et al. (1992). There exist two occultation observations (Wasserman et al. 1979; Dunham et al. 1990) and some speckle data (Drummond & Hege 1989). We adopted the most accurate $2a$ value (Dunham et al. 1990). The results for the minor axis $2b$ and $2c$ vary significantly and do not agree within the given error bars. In order to match all lightcurve observations we accepted the a/b and b/c ratios and the spin-vector from a lightcurve analysis (Erikson 1998, P. Magnusson, priv communication, 1997).

3 Juno Piironen et al. (1997) presented HG-fits for Juno based on several recent apparitions and derived reliable weighted means. The asteroid cross section has been directly determined during an occultation event (Millis et al. 1981) and with speckle interferometry (Baier & Weigelt 1983). The values of the calculated largest axis $2a$ agree within $1\,\%$, but in both cases no b/c has been determined. We put the $2a$ occultation value in Table 1 in parenthesis since it is only related to an instantaneous cross section and not to a full 3-dimensional ellipsoid. The shape and spin vector are in accordance with the available lightcurve data (Erikson 1998, P. Magnusson, priv communication, 1997).

4 Vesta For Vesta we combined the HG results from Piironen et al. (1997), Lagerkvist et al. (1992) and Lagerkvist & Magnusson (1990). There are several publications about occultation measurement (Dunham 1991), speckle observations (Schertl et al. 1995; Tsvetkova et al. 1991) and a combination of different methods (Drummond et al. 1988; Mc Carthy et al. 1994) with a reasonable agreement in results of size and shape. From Hubble Space Telescope images it has, however, been possible to determine the spin vector and detailed shape of Vesta (Thomas et al. 1997, see also "note added in proof"). The derived detailed shape model is available from a WWW-page (Stooke 1997), and was used instead of an ellipsoid. Binzel et al. (1997) derived a relative albedo map of the Vesta surface. Since there are no absolute albedo values assigned, it is not possible to apply it in our procedure. The albedo variations will cause a different temperature distribution on the surface and correspondingly alter the flux. Since the far IR fluxes are dominated by the cross section at the time of the observation, it will only be a second order effect in our aimed wavelength range beyond $50\,\mu\mathrm{m}$.

10 Hygiea Piironen et al. (1997) derived reliable HG-values based on 3 apparitions with observations at very small phase angles. The shape and spin vector are taken from Erikson (1998) and P. Magnusson (priv. communication). For Hygiea is only a single-chord occultation with a lower limit for the diameter available (D. Dunham, 1997, priv. communication).

54 Alexandra For Alexandra we use a default value of $G = 0.04$ based on its taxonomic type (Lagerkvist & Magnusson 1990). Under that assumption it was possible to calculate a mean H value from normalised magnitudes given in Belskaya et al. (1993). The shape and spin vector are taken from Belskaya et al. (1993), Erikson (1998) and P. Magnusson (priv. communication, 1997). There exists no published direct diameter value.

65 Cybele The H and G are taken from Lagerkvist & Magnusson (1990), with H as the mean value of 4 apparitions. Taylor (1981) published a low quality occultation observation of Cybele with only 3 chords over the full cross section, the $2a$ value in Table 1 is therefore in parenthesis. The shape and spin vector are taken from Erikson (1998).

106 Dione For Dione we use a default value of $G = 0.09$ based on its taxonomic type (Lagerkvist & Magnusson 1990). The absolute magnitude H has been calculated to $7.30\,\mathrm{mag}$ (A. Erikson, priv. communication, 1998). The major axis $2a$ is taken from one occultation measurement (Kristensen 1984). Since there exists no spin-vector solution we take a default spin-vector of $\lambda_\mathrm{p} = 0°$ and $\beta_\mathrm{p} = 90°$, and assume $a/b = 1.0$ and $b/c = 1.34$ to reproduce the occultation cross section and to avoid artificial lightcurve variations.

313 Chaldaea The Chaldaea H, G values as well as the shape and spin-vector are given in Erikson (1998). There exists no published direct diameter value.

532 Herculina Lagerkvist et al. (1992) derived H and G values based on four apparitions. For H we calculated the mean magnitude. The available occultation measurement produced only a 2-dimensional cross section (Bowell et al. 1978), whereas a sequence of speckle observation (Drummond et al. 1985) lead to a 3-dimensional ellipsoidal shape model. In Table 1 we included (in parenthesis) the largest axis $2a$ from the speckle results. The shape and spin-vector information is in agreement with the lightcurve observations (Michalowski 1996).

4. Observational photometric data

Our data sets contain thermal emission observations from 7 to $2\,000\,\mu\mathrm{m}$, taken from 1983 to 1997. We have individual photometric points as well as multi-filter photometry and thermal lightcurve measurements. The observation geometries include phase angles from $-30°$ to $+30°$, with negative angles related to *after* opposition and positive angles related to *before* opposition.

Table 1. Size, shape, spin-vector and magnitude input parameters. The values are based on direct measurements and lightcurve observations. The asteroids are divided into primary (top) and secondary (bottom) targets, as discussed in the text. The values in parenthesis are considered to be less reliable.

Asteroid	$2a$ (km)	a/b	b/c	$\lambda_{\rm p}$ (°)	$\beta_{\rm p}$ (°)	$P_{\rm sid}$ (days)	γ_0 (°)	JD_0	H (mag)	G
1 Ceres	959.2	1.00	1.06	0	90	0.378091	86	2440587.5	3.28	0.05
2 Pallas	574.0	1.10	1.25	45	−15	0.32555136	81	2440587.5	4.09	0.08
4 Vesta	578.0	1.03	1.22	319	59	0.2225887	344	2440587.5	3.20	0.34
532 Herculina	(263.0)	1.21	1.20	295	36	0.391872	6	2442413.5	5.89	0.16
3 Juno	(290.0)	1.21	1.20	108	36	0.300397	5	2440587.5	5.28	0.31
10 Hygiea	–	1.29	1.18	294	−35	1.150974	105	2444239.5	5.44	0.22
54 Alexandra	–	1.31	1.00	290	55	0.292766	42	2443906.5	7.48	0.04
65 Cybele	(260.0)	1.04	1.00	56	−25	0.2572901	−37	2446409.5	6.69	0.09
106 Dione	(170.4)	1.00	1.34	0	90	0.58	–	–	7.30	0.09
313 Chaldaea	–	1.21	1.20	234	44	0.3497707	47	2446630.5	8.79	0.05

We converted the available filter photometry to monochromatic fluxes at the *effective* or the *isophotal* wavelengths (Golay 1974). This allowed us to compile data from a number of references in a uniform format. Each entry i in the database consists of:

NR_i	the asteroid number
t_i	time of observation (Julian date)
λ_i	wavelength [μm]
$F_{{\rm o},i}$	observed monocromatic flux [Jy]
$\sigma_{{\rm o},i}$	estimated error [Jy]

where $1\,{\rm Jy} = 10^{-26}\,{\rm W\,m^{-2}\,Hz^{-1}}$.

The database contained 678 individual observations in December 1997, and because of its size it is only available in electronic format[7]. A quantitative summary of all measurements is given in Table 2. In the following we describe the data sets per instrument or telescope.

4.1. IRAS data

In 1983 IRAS[8] surveyed the sky in 4 wavelength bands centred at 12, 25, 60 and 100 μm (Neugebauer et al. 1984). Photometry for more than 1 800 asteroids has been obtained during the mission time. A description of the data products can be found in *The IRAS Minor Planet Survey (IMPS)* (Tedesco 1992). Starting from the IMPS table No. 108, we applied colour corrections to obtain monochromatic fluxes at 12, 25, 60 and 100 μm. In cases where the S/N was lower than 10 a *flux overestimation correction* (Tedesco et al. 1992) has been applied. We ignored the *Band-to-Band* corrections. They have been introduced by Tedesco et al. (1992) in order to bring the individual diameters and albedos, derived with the STM for each band flux, into agreement. According to the IMPS the measurement errors are between 10 and 25 %. Some Ceres observations are already in the non-linearity range of the detectors and therefore questionable, we excluded them. The *IRAS Explanatory Supplement* (Beichmann et al. 1988) gives an additional absolute band uncertainty of 2 % (12 μm), 5 % (25 μm), 5 % (60 μm) and 10 % (100 μm). Cohen et al. (1996) conclude from a statistical comparison of IRAS photometry with models for 12 bright standard stars that, at 12 μm and 25 μm, flux densities measured by IRAS should be revised downwards by about 4.1 % and 5.7 %, respectively. We root-sum-squared the stated errors.

4.2. JCMT data

All JCMT observations have been obtained during several observing runs with the UKT14[9]-Bolometer (Duncan et al. 1990) between September 1989 to April 1996. The last campaign in April 1996 took place in support for the ISO mission (D. Hughes, J. Stevens, priv. communication). All data are available from the JCMT archive (http://cadcwww.dao.nrc.ca/jcmt). The standard data reduction is described in Redman et al. (1992) or in Emerson (1994). In principle the measured signal is multiplied by the flux conversion factor, which is based on calibration measurements. The extinction can be obtained from the τ-meter at CSO[10]. Colour corrections are not relevant. The overall uncertainty is derived from the S/N-ratio, the data reduction process and the absolute errors of the submillimetre calibrators. Typical total uncertainties are in the order of 10 to 20 %.

4.3. UKIRT mid-IR N and Q data

During the ISO mission several observing campaigns have been performed at the UKIRT with the 128 × 128 *Si:As*-BIB[11] MAX[12]-Camera from the MPIA[13] (http://www.mpia-hd.mpg.de/MPIA/Projects/IRCAM/MAX/index.html). We obtained N and Q band photometry in chopping-nodding mode

[7] Table 7 is available via anonymous ftp to cdsarc.u-strasbg.fr (130.79.128.5) or via http://cdsweb.u-strasbg.fr/Abstract.html

[8] Infrared Astronomical Satellite

[9] United Kingdom Telescope, Cryostat No. 14

[10] Caltech Submillimeter Observatory

[11] Blocked Impurity Band

[12] **M**id-Infrared **A**rray e**X**pandable

[13] Max-Planck-Institute für Astronomie, Heidelberg

for all 10 asteroids and parts of thermal lightcurves for selected targets. The definition of the photometric system, including instrumental and celestial calibration, has been established in collaboration with M. Cohen, Berkeley (private communication, 1997). A full description of the data reduction process can be found in Müller (1997), including passbands, calibration stars and error calculation. The highest quality N and Q band results have a relative uncertainty of less than $5\,\%$, the absolute total errors are at 8 to $15\,\%$.

4.4. IRTF mid-IR N and Q data

The STM was calibrated by Lebofsky et al. (1986), based on K, M, N and Q band measurements on Ceres and Pallas. Here we consider only the N and Q band data, where the flux contribution from reflected light is negligible. We applied the given colour correction factors to obtain monochromatic fluxes at the central filter wavelengths. The stated accuracy of 1–5 % in Lebofsky et al. (1986) seems to be too optimistic considering the fact that the absolute photometric system at N and Q is only known to 3–5 % (Rieke et al. 1985). Adding a photometric system offset of $3\,\%$ (Hammersley et al. 1998) and typical atmospheric variations during the nights, we ended up at around $10\,\%$ uncertainty for the highest quality data. This is roughly equivalent with increasing all published uncertainties by a factor of 3.

4.5. ISOPHOT

ISOPHOT performed observations of photometric standards on a weekly basis to calibrate the internal flux reference (FCS[14]). At wavelengths beyond $50\,\mu\mathrm{m}$ it is necessary to observe stars, asteroids and planets to cover the full dynamic range of the detectors. The selected 10 asteroids provide the intermediate flux interval (see Fig. 1). It is possible to deselect all asteroid observations from this calibration program and base the determination of the FCS at high flux levels only on the planets and at low flux levels only on stars. The asteroid measurements can then be treated as independent scientific observations (Müller 1997). The bright ones can be compared against the planets Uranus and Neptune, whereas the faint ones are close to flux densities of the brightest standard stars. The internal reference source FCS allows a comparison of observations, taken at different epochs. The observing mode of centring the source on each detector pixel provides in case of C100 (9 pixels) and C200 (4 pixels) several independent measurements of the same object within a few minutes. The observing sequence is accompanied by background and dark current measurements, leading to reliable asteroid fluxes with an uncertainty of $10\,\%$. All measurements are exclusively calibrated against well known standard stars and planets. Examples for this method and a discussion of the possibilities, as well as the limitations can be found in Müller (1997). In total we derived 35 individual photometric data points between 50 and $200\,\mu\mathrm{m}$.

[14] Fine Calibration Sources

Table 2. Data coverage per instrument and asteroid NR. Summary of the number of data points selected (Sect. 5.3) in the analysis, from the data set available in December 1997.

	Instrument					
NR	IRAS	JCMT	UKIRT	IRTF	ISOPHOT	HHT
1	0	49	9	22	6	1
2	27	10	9	10	3	0
4	3	82	18	0	2	0
532	21	15	51	0	2	0
3	32	0	17	0	4	0
10	34	1	25	2	5	0
54	20	0	2	0	2	0
65	24	0	4	0	8	0
106	24	2	17	0	1	0
313	24	4	15	0	2	0

4.6. Other data

Altenhoff et al. (1996) measured the intensity ratio of the planet Mars and the asteroid Ceres at a frequency of $250\,\mathrm{GHz}$ with a wideband bolometer at the HHT[15] (Kreysa 1990; Baars & Martin 1990; Martin & Baars 1990). From 58 pairs of observations they derived at $1\,200\,\mu\mathrm{m}$ a flux density ratio of Mars and Ceres of 268.5, corrected for the partial resolution of Mars. The brightness variation with the rotation phase was smaller than $\pm 2\,\%$. They claim that their obtained flux density has an accuracy of better than $3\,\%$, but adding the Mars uncertainties of $5\,\%$ we get a total error of $6\,\%$ for those Ceres observations.

5. Methods

The input and observational data discussed in Sects. 3 and 4, vary significantly in coverage and quality for the different objects. Therefore the ten asteroids were classified into two groups of so-called primary and secondary calibrators. The requirements for the primaries are: 1) good and high quality data coverage from $10\,\mu\mathrm{m}$ to sub-mm wavelengths, 2) well determined physical dimensions from stellar occultations or other direct measurements, 3) well known spin vectors. The asteroids Ceres, Pallas, Vesta, Herculina were selected to be primaries, and the remaining ones to be secondaries. It is, however, clear that there are still significant differences in quality within these groups.

In order to use asteroids as calibrational standards in the far-IR it is necessary to know their fundamental thermophysical properties. The model parameters to be determined are: the thermal inertia Γ, the beaming parameters ρ and f, and the wavelength dependent emissivity $\varepsilon_{\mathrm{h}}(\lambda)$. For some of the secondaries it is also necessary to determine the size $2a$ and albedo p_V.

To clearly separate and distinguish between the various effects introduced by these parameters, it is necessary to have enough high quality data to do good statistics. The approach here is to use various statistical methods on the data for the primary asteroids, to derive their thermophysical parameters. Then,

[15] Heinrich-Hertz-Telescope

from these results a set of "default" parameters are suggested for the secondaries .

Statistical measures are introduced to compare the observations with the model. Ideally one would optimise all model parameters simultaneously to achieve the best possible fit, but this would be a very time consuming and complex process. The approach here is to optimise the parameters separately, and then iterate between the steps to obtain a global solution.

5.1. Data analysis

For a given set of parameters the model predicts a flux $F_{\mathrm{m},i}$, which should be compared to the observed flux $F_{\mathrm{o},i}$. A least-square approach would be to optimise the sum of $(F_{\mathrm{o},i}-F_{\mathrm{m},i})^2$ over the available data points i. This would, however, strongly weight the mid-IR data, since the absolute flux varies significantly with wavelength. To avoid this we scaled the data by

$$r_i = F_{\mathrm{o},i}/F_{\mathrm{m},i} \qquad \text{and} \qquad \delta r_i = \sigma_{\mathrm{o},i}/F_{\mathrm{m},i} \tag{2}$$

Let $\mathcal{D}$ be some selected subset of the database. If the data are weighted by for example $w_i = 1/\delta r_i^2$, the least-square method can be formulated as the optimisation of

$$L = \sum_{i\in\mathcal{D}} w_i (r_i - 1)^2 \Big/ W_{\mathcal{D}} \qquad \text{where} \quad W_{\mathcal{D}} = \sum_{i\in\mathcal{D}} w_i \tag{3}$$

By weighting the data it is possible to somewhat compensate for some of the inconsistencies in the database. There are, however, also inconsistencies in the relative errors between different investigations. This can be taken into account by correcting $w_i = 1/\delta r_i^2$ with some factor, depending on which instrument and investigators the data originate from.

Due to the large dimension of the parameter space to be optimised, it is very useful to consider some preparatory steps. The weighted mean and standard deviation of the ratios are defined by

$$\langle r\rangle_{\mathcal{D}} \;=\; \sum_{i\in\mathcal{D}} w_i r_i \Big/ W_{\mathcal{D}} \tag{4}$$

$$\sigma^2_{\mathcal{D}} \;=\; N_{\mathcal{D}} \sum_{i\in\mathcal{D}} w_i \big(r_i - \langle r\rangle_{\mathcal{D}}\big)^2 \Big/ (N_{\mathcal{D}}-1) W_{\mathcal{D}} \tag{5}$$

where $N_{\mathcal{D}}$ is the number of data points in the subset $\mathcal{D}$. It is possible to "sub-optimise" a group of parameters by searching for $\langle r\rangle_{\mathcal{D}} = 1$, or by minimising $\sigma_{\mathcal{D}}$. Typically, as a starting point, one or a few parameters are varied while the others are fixed. The undetermined fixed parameters will cause temporary bias effects, which to some extent can be avoided by separately studying either the mean or the standard deviation of the ratios.

5.2. Derivation of thermophysical parameters

As described above parameter subsets are optimised separately. It is also useful to start with the most important properties, before tuning the finer details of the model. Determining the size and albedo is therefore the first step, since the flux is proportional to the diameter squared. The beaming and heat conduction are then treated together, since they have both competing and complementary effects on the thermal emission. The tuning of the emissivity is the last step, because the procedure is relatively easy to handle without major recalculations. By proceeding in this order, it is possible to keep the number of iterations between these steps to a minimum, before reaching a final and self-consistent solution.

5.2.1. Diameter and Albedo

The observed visual magnitude of an asteroid does not immediately give its size since the object can be either large with a dark surface, or small with a bright surface. Formally this is expressed as

$$\log p_V = 6.259 - 2\log D_{\mathrm{eff}} - 0.4H \tag{6}$$

where D_{eff} is the (effective) diameter (Bowell et al. 1989). For near spherical objects this is unambiguous, but for more elongated objects the dimensions specified in Table 1 have to be related to D_{eff}. For simplicity we take the effective diameter to be the diameter of the equal volume sphere. For the ellipsoids this is $D_{\mathrm{eff}} = 2(abc)^{1/3}$.

Since the goal is to achieve a self-consistent set of parameters, Eq. (6) is solved to give p_V for the primary asteroids, for which there are direct size measurements. If there is no independent size estimate, one more constraint needs to be added. Since the thermal IR flux is proportional to D^2_{eff}, it is possible to write

$$D_{\mathrm{eff},i} = D_{\mathrm{eff}}(\mathrm{guess}) \cdot \sqrt{F_{\mathrm{o},i}/F_{\mathrm{m},i}} \tag{7}$$

where the model flux $F_{\mathrm{m},i}$ is based on some guessed D_{eff} and p_V. Combined, Eqs. (6) and (7) gives a solution $(D_{\mathrm{eff},i}, p_{V,i})$, which is illustrated in the albedo vs. diameter diagram in Fig. 2.

For a given asteroid and data set, the weighted mean and standard deviation of the derived effective diameters are computed. The weights used in this case are $w_i = (F_{\mathrm{o},i}/\sigma_{\mathrm{o},i})^2$, since the diameters (and thus $F_{\mathrm{m},i}$) are not known *a priori* for some of the objects.

5.2.2. Thermal inertia and beaming

The thermal inertia influences the IR emission in primarily two different ways. Increasing the Γ means more night side emission at the expense of the day side emission. Since main-belt asteroids only can be observed at phase angles lower than about 30°, the inertia almost always lowers the expected flux. This is most pronounced in the mid-IR, close to the emission peak. On the other hand in the far-IR the emission is significantly less sensitive to the temperature decrease due to the thermal inertia. Typically the difference in flux between zero and a reasonable asteroid thermal inertia is $\sim$ 10–20 % in the mid-IR and less than $\sim$ 1–2 % in the far-IR.

The thermal inertia also causes the observed asymmetry in the thermal IR phase curves, before and after opposition (Morrison 1977; Hansen 1977; Lebofsky et al. 1986). This is because of the flux difference between the cooler morning side

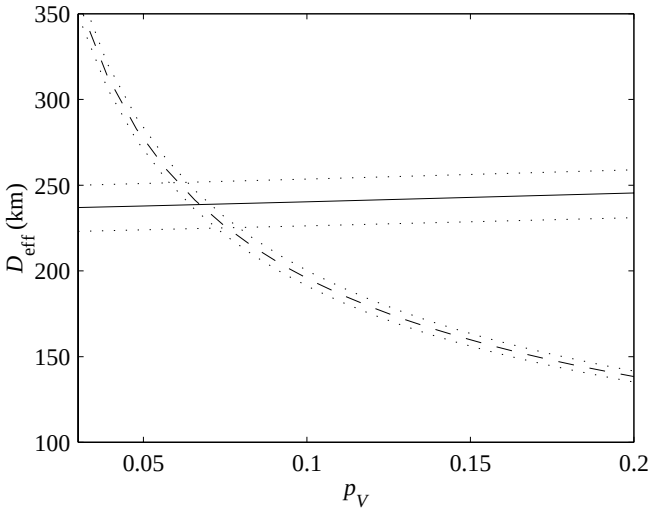

Fig. 2. The albedo and diameter of 65 Cybele. The dashed line is the constraint from $H = 6\overset{\rm m}{.}69$, and Eq. (6). The solid line is the constraint from one $12\,\mu$m IRAS observation. The dotted curves indicates the error envelopes of the two curves, based on a assumed error of $\pm 0\overset{\rm m}{.}05$ for the H-parameter and the flux error given for the IRAS observation. The intersection of the two curves gives the best solution for the parameter set $(D_{{\rm eff},i}, p_{V,i})$

and the warmer afternoon side. For a prograde rotator at higher phase angles, the mid-IR flux can be $\sim$ 5–15 % brighter before than after opposition. Again, the effect decreases towards longer wavelengths.

The beaming is the observed tendency of the thermal emission to be directed stronger towards the solar direction at the expense of the emission at larger phase angles. The approach to explain the beaming effect by surface roughness predicts that the brightness temperature should be fairly constant over a wide wavelength range (Lagerros 1998). Due to the non-linear behaviour of the Planck function at shorter wavelengths the effect is strongest in the mid-IR. For example, the $10\,\mu$m flux is typically a factor $\sim$ 20–40 % larger than predicted for a smooth Lambertian surface. In the far-IR the correction is less than 10 %.

For determining the thermal inertia Müller (1997) suggested a technique to compare the mean ratios $\langle r \rangle_{\mathcal{D}}$ before and after opposition. By varying the model thermal inertia Γ, these values should come to an agreement. If there are systematic effects left due to other parameters still being ill-determined, the agreement does not necessarily need to be at $\langle r \rangle_{\mathcal{D}} = 1$.

Another possibility is to compute ratios r, using a model inertia $\Gamma = 0$. The slope of $r = r(\alpha)$, for phase angles α, could then be compared to predicted model slopes for different thermal inertias. Again, the method should be insensitive to, for example, the diameter not being well determined.

The problem with these and other methods is, however, the need of a good wavelength and phase angle coverage, both before and after opposition. Furthermore, the beaming and thermal inertia cause competing effects which can be hard to separate at mid-IR wavelengths.

The brute force approach here is to use the least-square method in Eq. (3). The model parameters Γ, ρ, and f are varied over a three dimensional grid in search for the least-square solution. For a derived solution, the mean and standard deviation of the model ratios r_i are also computed as a consistency check.

5.2.3. Wavelength dependent emissivity

The emissivity depends both on composition and bulk properties of the surface material. Various minerals have several molecular bending, stretching, and crystal lattice vibrational modes in the mid- and far-IR. Subsurface scattering processes in the porous regolith affect the emission. The emissivity depends on the particle size distribution, as compared to the observed wavelength. The current model does not describe these processes in detail. The emissivity is taken to be a function dependent on wavelength, to be fitted to the data.

The far-IR flux is to a good approximation directly proportional to the hemispherical $\varepsilon_{\rm h}(\lambda)$ (the emissivity used in the model is strictly speaking dependent on the direction). The approximation is to some extent valid at shorter wavelengths, but altering the mid-IR emissivity will also change the temperature. For a given set of model parameters, it is possible to define the "observed emissivity" for a data point i as:

$$\varepsilon'_{\rm h}(i, \lambda_i) = \varepsilon_{\rm h}(\lambda_i) r_i \tag{8}$$

The corresponding "error" in the observed emissivity is taken to be $\delta\varepsilon'_{\rm h} = \varepsilon_{\rm h}(\lambda_i)\delta r_i$.

Given the scatter between the dataset, which is in many cases larger than the individual errors, it is not advisable to fit a detailed emissivity model to all specific wavelengths in the database. To improve the statistics the data is divided into a small number of wavelength bins. The weighted mean of observed emissivities is computed for each bin, and is attributed to the mean wavelength $\langle \lambda_i \rangle$ of that bin (Müller 1997). A cubic interpolation is then used to derive a smooth curve connecting these points in the wavelength – emissivity diagram.

5.3. Data selection

By deriving diameters and albedos from photometric data points it became clear that some individual observations are of poor quality and that assigned uncertainties are too small. We compared radiometric diameters with the results from direct methods to show that there is a general agreement between both numbers (within 10 %). Afterwards we deleted observations where the radiometric $D_{{\rm eff},i}$ differed by more than 2σ from $\langle D_{\rm eff} \rangle$ (Table 3). This selection procedure concerned only a very small number of observations where we believe that they are due to typing errors in the original references, or undetected effects during the observations.

We also ignored IRAS observations of Ceres due to the large uncertainty (Matson & Tedesco 1992) and the large offset between radiometric $D_{{\rm eff},i}$ and $\langle D_{\rm eff} \rangle$.

6. Results

The dataset is very inhomogeneous in terms of coverage and quality. The detailed analysis of the individual parameters, however, requires a more homogeneous dataset. The data points of lowest quality were therefore discarded according to Sect. 5.3. The number of data points used in the following analysis is summarised in Table 2.

The inversion methods outlined in Sect. 5.1 were applied to the select data points. The various groups of parameters were sub-optimised separately, and in order to obtain a "global" solution it was necessary to iterate through these steps a few times. Using the final results the data selection was applied once more as a consistency check. The selected data set remained exactly the same.

6.1. Direct versus radiometric size

In Table 3 we compare the effective diameters, calculated from the direct measurements in Table 1 (and using $D_{\rm eff} = 2(abc)^{1/3}$), with the derived radiometric diameters. For Ceres, Pallas and Vesta the real size has been determined from several independent direct measurements with self-consistent results. The effective radiometric diameters agree within $0.7\,\%$ (Ceres), $0.2\,\%$ (Pallas) and $0.6\,\%$ (Vesta) with the real diameters. This confirms that the set of model parameters is self-consistent for the objects and that the input parameters are reasonable. On the other hand, for Juno and the other secondaries, the radiometric diameters are independent of the available direct diameters, since they are not used at all in the modelling.

For Herculina there exists a 3-dimensional ellipsoidal model, but only based on speckle observations without any direct confirmation from an occultation. On the other hand the radiometric diameter is based on 89 individual observations. We therefore accept the radiometric solution, since the speckle results have not the same quality as the occultation results. Juno, Cybele and Dione also have direct occultation measurements, but only with a cross section determination at one single time. For all three it is therefore advisable to use the radiometric solutions based on large numbers of observations with different viewing geometries. For Hygiea, Alexandra and Chaldaea no comparison with direct observations can be made.

The given uncertainties in the radiometric $D_{\rm eff}$ are reflecting the scatter in the size determinations from individual observations. They comprise changing cross sections due to the shape and the rotation of the asteroids, as well as the observational uncertainties. The corresponding albedo has been calculated with equation 6 for direct and radiometric diameters. The boldface values are used as input parameters for the TPM. In the last column of Table 3 we calculated radiometric diameters with the STM by using the recommended correction factors (Lebofsky et al. 1986). Although the produced values are on average acceptable, the larger scatter in the diameters indicates that the predicted fluxes at a specific point in time can be unacceptable. The case of Pallas demonstrates that also the absolute fluxes from the STM can be significantly different (a $10\,\%$ diameter change produces roughly a $20\,\%$ flux change).

6.2. Thermal inertia

Due to the large observational uncertainties and the limited data samples our methods are only indicative for the determination of the thermal inertia. All approaches show clearly that the thermal inertia is much smaller than the lunar value of $50\,{\rm J\,m^{-2}\,s^{-0.5}\,K^{-1}}$ (Spencer et al. 1989). The total flux level as well as the asymmetry in thermal phase curves lead to a lower limit of about $10\,{\rm J\,m^{-2}\,s^{-0.5}\,K^{-1}}$.

The thermal inertia was optimised together with the surface roughness parameters. The optimisation along the thermal inertia axis is illustrated in Fig. 3, where the optimal values for ρ and f are used (see Sect. 6.3). In case of Ceres the minimum in Fig. 3 is most pronounced. The spin vector of Ceres is close to perpendicular to the line of sight, and the wavelength as well as the phase angle coverage is quite good. For objects with worse data coverage or spin vectors close to the orbital plane, the results are less conclusive, as is seen in Fig. 3.

The individual Γ for the primaries are between 5 and 25. For our secondary standards we use a default of $\Gamma = 10\,{\rm J\,m^{-2}\,s^{-0.5}\,K^{-1}}$. The least-square method for Γ in combination with the surface roughness parameters resulted in the individual thermal inertias given in Table 4.

6.3. The surface roughness parameters

The beaming parameters ρ and f have been determined together with the thermal inertia (Table 4). They represent therefore the best solutions of the least-square method, including all observational data. If heat conduction is neglected, the surface roughness approach produces a beaming effect in agreement with the "default" STM beaming parameter (Lebofsky et al. 1986), at $\rho \sim 0.6$–0.8 and $f \sim 0.6$ (Lagerros 1998). With the thermal inertia taken into account, a rougher surface is needed in order to produce the same amount of beaming. A total crater coverage of the asteroid surface ($f = 1.0$) is perfectly acceptable, since the crater definition includes also "micro" craters at the smallest possible scale. The ρ parameter varies between 0.8 and 1.4. If we take the uncertainties of the most important mid-IR data, especially ground-based Q-Band photometry, into account then the resulting beaming parameters are in agreement with the theoretical considerations of Lagerros (1998). We expect that the beaming model can be improved in the near future with the release of ISO data, mainly thermal spectra at mid-IR wavelengths. In fact, first comparisons of the new model with ISOSWS data (A. Salama, priv. communication, 1998) and with KAO[16] spectra (Cohen et al. 1998) indicate that the derived ρ and f-values are slightly too high in the case of Ceres. Cohen et al. (1998) report the presence of three emissivity features in Ceres which may affect the determination of the underlying spectral shape from ground-based N-band photometry, which

[16] Kuiper Airborne Observatory, NASA

we used here. Smaller beaming parameters would change the spectral shape of the Wien-part of the spectrum, but do not influence the FIR, where the asteroids are used as photometric standards.

6.4. Wavelength dependent emissivity

LeVan & Price (1984) found a decrease in emissivity from 20 to 85 μm for 4 asteroids. This is in qualitative agreement with both observational and theoretical investigations of the emissivity characteristic of lunar soil particle size distribution (Simpson et al. 1981). Redman et al. (1992) calculated a lower Rayleigh-Jeans temperature at submillimetre wavelength compared to the mid-IR or to the centimeter region. They suggest that this is an indication for the presence of a dusty, porous regolith. Scattering processes by grains within the regolith reduce the emissivity in a wavelength dependent fashion. We follow this interpretation. In Fig. 4 we plotted the "observed" emissivity as defined in Sect. 5.2.3. A clear trend of decreasing emissivity towards longer wavelengths can be seen. All primaries, except Vesta, show a similar behaviour. Neither changes in the beaming model nor in the thermal inertia can account for the increase in emissivity from 10 to 20 μm. The explanation for this phenomenon will require additional investigations, but could be due to transparency features. With the increase of the transparency of the material at some wavelength it is possible for deeper and warmer layers to contribute to the thermal emission. Longward of 20 μm the emissivity becomes smaller, reaching levels of below 0.8 in the submillimetre. In case of Vesta we find emissivities as low as 0.6. This is in agreement with the results of Redman et al. (1992). We summarized the results in Table 5.

We see this trend of $\varepsilon_{\rm h}(\lambda) < 0.9$ in the submillimetre for all primaries. Since we do not have large samples of good quality observations in the far-IR beyond 50 μm, it could well be that the emissivity drops already at shorter wavelengths. Preliminary analysis of Ceres-spectra, taken with ISOLWS, indicate a lower $\varepsilon_{\rm h}$ beginning at 100 μm (T. Lim, priv. communication, 1998).

7. Discussion

The full thermophysical treatment allows us to understand the thermal behaviour and to explain the observations in our database. We tested the model also against additional preliminary IRTF and KAO data (C. Telesco, D. Osip, priv. communication) and ISOLWS[17] spectra (M. Burgdorf, priv. communication). All test cases confirmed the quality of the TPM on absolute and relative levels. We can now predict flux densities from mid-IR to submillimetre wavelengths for all 10 asteroids, including thermal and lightcurve effects. In that way we defined photometric standards for different photometric applications.

7.1. Accuracy of the individual standards

The best proof for the reliability of a theoretical model is the test against validated observations. We calculated the TPM flux for each data point in our database and compared observations and predictions one by one. We grouped afterwards the resulting ratios in certain wavelength bins (see Table 6) and analysed the weighted means $\langle r \rangle$ and the weighted r.m.s. of $(r_i - 1)$. The results are summarized in Table 6. Our primary standards Ceres, Pallas, Vesta and Herculina show in the ISOPHOT far-IR range a r.m.s. of about 10 %. Since for the neighbouring regions similar r.m.s. are derived, we conclude that the TPM prediction for a given time will be better than 10 %. The scatter for the secondaries is larger, but in all cases, except Dione and Cybele, below 15 %. The r.m.s. values in table 6 represent the expected uncertainties when using the asteroids for photometric

[17] ISO Long-Wavelength Spectrometer

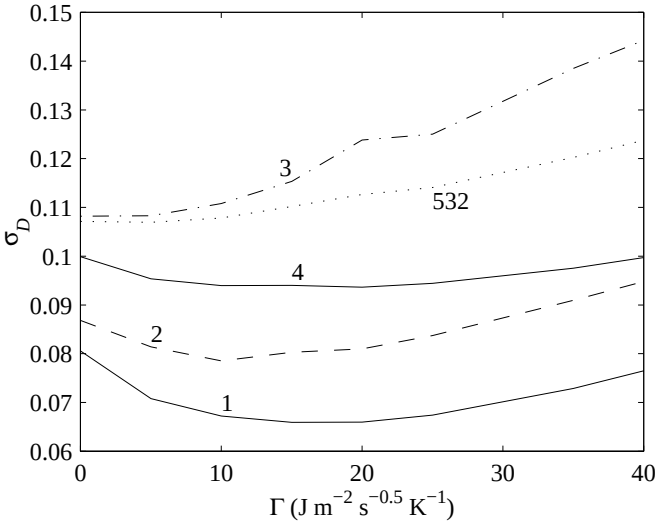

Fig. 3. Determining the thermal inertia Γ of 1 Ceres, 2 Pallas, 3 Juno, 4 Vesta, and 532 Herculina, by optimising the weighted standard deviation $\sigma_{\mathcal{D}}$. The curves are computed for the ρ and f parameters given in Table 4.

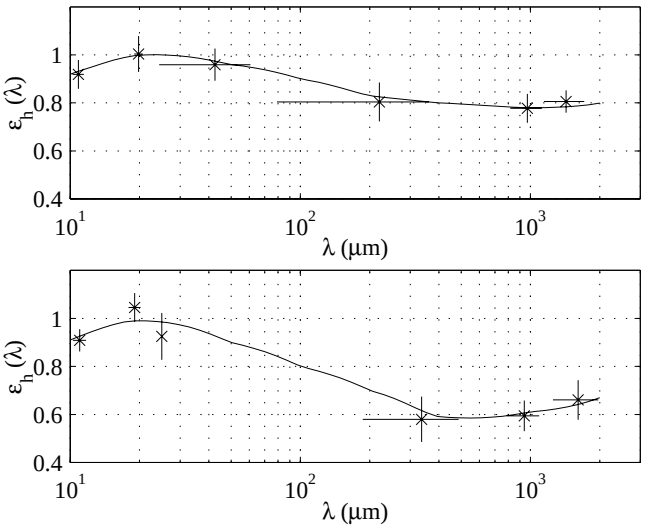

Fig. 4. The wavelength dependent emissivity $\varepsilon_{\rm h}(\lambda)$. The upper panel is the combined results of 1 Ceres and 2 Pallas, and the lower panel is for 4 Vesta.

Table 3. Effective diameters and albedos. The "direct" diameters are derived from $D_{\rm eff} = 2(abc)^{1/3}$ and the values in Table 1. The weighted mean and standard deviation (in parenthesis) of the derived radiometric diameters are given. STM radiometric diameters $D_{\rm STM}$ are also derived for comparison. All albedos are calculated from Eq. (6). The values adopted for the model are indicated in bold face.

	Direct		Radiometric		
NR	$D_{\rm eff}$ (km)	p_V	$D_{\rm eff}$ (km)	p_V	$D_{\rm STM}$ (km)
1	**922.7**	**0.104**	929.0 (31)	0.103	938.8 (33)
2	**500.0**	**0.168**	499.0 (19)	0.169	564.0 (43)
4	**530.4**	**0.339**	533.5 (24)	0.335	537.6 (29)
532	218.0	0.168	**207.3** (12)	**0.186**	208.3 (17)
3	240.3	0.243	**241.4** (12)	**0.241**	238.1 (14)
10	–	–	**429.9** (32)	**0.066**	420.4 (46)
54	–	–	**161.6** (12)	**0.071**	162.9 (8)
65	253.3	0.060	**258.8** (25)	**0.057**	258.9 (21)
106	154.6	0.091	**180.8** (27)	**0.067**	170.2 (26)
313	–	–	**91.0** (6)	**0.067**	101.2 (6)

Table 4. Derived physical properties. The thermal inertia Γ is given in $\mathrm{J\,m^{-2}\,s^{-0.5}\,K^{-1}}$. The surface roughness is described by the crater coverage fraction f, and the r.m.s. slope ρ.

NR	Γ	ρ	f
1	10	1.4	1.0
2	10	1.2	1.0
4	25	1.2	1.0
532	15	0.8	0.6
3	5	1.4	1.0
Default	10	1.2	1.0

Table 5. The hemispherical emissivity $\varepsilon_{\rm h}(\lambda)$ in the wavelength range $\lambda = 10$–$2\,000\,\mu$m.

10	20	50	100	200	400	1 000	2 000
4 Vesta:							
0.91	0.99	0.90	0.80	0.70	0.59	0.61	0.67
Default:							
0.92	1.00	0.96	0.90	0.83	0.80	0.78	0.80

calibration. The table shows also deficiencies in observations for individual objects (i.e. Dione) and some wavelength regions, mainly the submillimetre.

As a final example, UKIRT Q-band data of Herculina are compared to model thermal light curves in Fig. 5. There are residual systematic differences in the absolute calibration of the two consecutive nights. Nevertheless, the model is able to predict the ligth curve variations without adding any offsets to the flux or shifting the time scale.

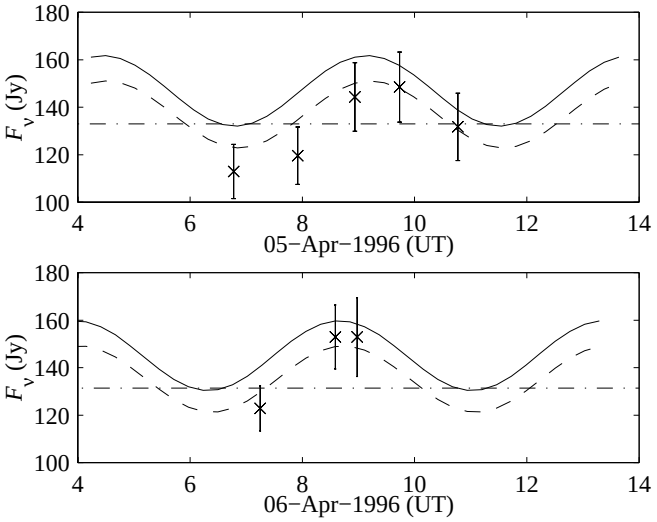

Fig. 5. Model and observed thermal light curves of 532 Herculina, at $\lambda = 19.94\,\mu$m. Lines are for $\Gamma = 0$ (solid), $\Gamma = 15$ (dashed), and STM (dot-dashed). There is no shift added to the absolute level of the model flux or the rotational phase in order to fit with these specific data points.

Table 6. The final weighted r.m.s. of $(r_i - 1)$ for 6 wavelength bands in the range 7–$2\,000\,\mu$m. That is, $\sqrt{L}$ calculated from Eq. (3).

NR	7–13	13–24	24–500	500–1 200	1 200–2 000
1	0.059	0.091	0.098	0.045	0.126
2	0.077	0.061	0.087	0.057	0.166
4	0.048	0.076	0.088	0.108	0.104
532	0.106	0.101	0.111	0.136	0.329
3	0.089	0.185	0.086	–	–
10	0.172	0.287	0.117	0.107	–
54	0.119	–	0.137	–	–
65	0.209	0.049	0.187	–	–
106	0.307	0.321	0.285	0.235	–
313	0.085	0.152	0.139	0.207	–

7.2. General limitations

Our results are related to the 10 calibration asteroids. But there are many aspects which are also true for other asteroids. Depending on the needs for future projects we can extend the possibilities for new photometric standards.

Taxonomic type More than about 90 % of all asteroids (Zellner & Bowell 1979) belong to either of the taxonomic types C ("carbonaceous") or S ("stony") (Tholen 1984; Barucci et al. 1987). By neglecting any subgroups, the asteroids discussed here are either C- or S-types, except for Vesta which forms a group of its own. It is, therefore, not unreasonable to expect the results obtained here to be applicable to most other main-belt asteroids. In future investigations we hope to include M-type ("metallic") asteroids, since they could be high thermal inertia candidates.

Shape of asteroids One criterion for the preselection of the objects was a small amplitude in the lightcurve to allow for long integration times without significant flux changes. In general the TPM is valid also for more elongated objects, but this has not been extensively tested.

Wavelength range We aimed at the ISOPHOT far IR flux calibration, and optimised for a best agreement in that range. In principle TPM covers the total thermal emission from near IR to the radio region. Since we did not include reflected light, the valid range begins at around $6\,\mu\mathrm{m}$ where the thermal emission dominates. The mm-range and beyond is also not well tested and needs further investigations.

Phase angle range TPM takes illumination geometry into account. In principle there are no limits for the phase angle range, but since all observations have been taken at phase angles smaller than 30°, we had no possibilities to test the validity of the model at large phase angles, as they occur for instance for near-Earth asteroids (NEA).

Time range The model parameters can of course be improved with more observational data. The only quantity, however, that is "degrading" with time is the timing of the lightcurves. Except for Dione, the spin vectors given here should be good enough for decades. In most cases, it will only take a few additional observations to update the spin period and the timing of the lightcurves. The model results can therefore be used for IRAS data as well as for future projects.

7.3. Outlook

The thermophysical model proves to be an excellent tool to explain thermal data from the near IR to submillimetre wavelengths. Nevertheless our derived input parameters are only the starting point and can be improved by higher quality data sets and by filling the wavelength-phase angle space for each object. Some asteroids need also more lightcurve observations to clarify the ambiguities in the spin-vector solutions.

The strong need for far-IR photometric standards between the stars and the planets is not limited to ISOPHOT. Other ISO instruments (LWS[18] and SWS[19]) have also large asteroid programmes for testing and improving their photometry (M. Burgdorf, A. Salama, priv. communications). First efforts to use the asteroids as photometric standards in the submillimeter (HHT[20], JCMT[21]) have started already. Future application for airborne (SOFIA[22]) and spaceborne (FIRST[23], SIRTF[24]) experiments can be expected.

Acknowledgements. We thank Claes-Ingvar Lagerkvist, Per Magnusson and Anders Erickson for their comments and support in discussions about the HG-parameters, shape and spin vector solutions. We thank also the members of the ISOPHOT Instrument Dedicated Team in Villafranca and the ISOPHOT Data Centre in Heidelberg, especially D. Lemke, U. Klaas, B. Schulz and S. Huth, for the helpful discussions about the ISOPHOT data reduction, many useful comments and the explanation of the FCS tables.

We retrieved the submillimetre data from the JCMT archive at the Canadian Astronomy Data Centre, which is operated by the Dominion Astrophysical Observatory for the National Research Council of Canada's Herzberg Institute of Astrophysics. We thank D. Hughes and J. Stevens for sharing their experience with the submillimetre instrumentation and the data reduction.

The UKIRT observations have been performed by the MPIA MAX instrument team, namely S. V. W. Beckwith, M. Robberto, T. Herbst and P. Bizenberger.

We also would like to express our thanks to the referee, Dr. M. Cohen. His comments were very helpful and improved the paper significantly.

References

Altenhoff, W.J., Baars, J.W.M., Schrami, J.B., Stumpff, P., von Kapherr, A., 1996, A&A 309, 953

Baars, G., Martin, R.M., 1990, in ESA, From Ground-Based to Space-Borne Sub-mm Astronomy (SEE N91-21986 13-89), pp 239-297, ESA

Baier, G., Weigelt, G., 1983, A&A 121, 137

Barucci, M.A., Capria, M.T., Coradini, A., Fulchignoni, M., 1987, Icarus 72, 304

Beichman, C.A., Neugebauer, G., Habing, H.J., Clegg, P.E., Chester, T.J., 1988, Infrared astronomical satellite (IRAS) catalogs and atlases. Volume 1: Explanatory supplement

Belskaya, I.N., Dovgopol, A.N., Erikson, A., Lagerkvist, C.I., Oja, T., 1993, A&ASS 101, 507

Binzel, R.P., Gaffey, M.J., Thomas, P.C. et al., 1997, Icarus 128, 95

Bowell, E., Hapke, B., Domingue, D., Lumme, K. et al., 1989, in R.P. Binzel, T. Gehrels and M.S. Matthews (eds.), Asteroids II, pp 524-556, The University of Arizona Press

Bowell, E., Hapke, B., Domingue, D. et al., 1989, in R.P. Binzel, T. Gehrels and M.S. Matthews (eds.), Asteroids II; Proceedings of the Conference, Tucson, AZ, Mar. 8-11, 1988 (A90-27001 10-91), pp. 524-556, Arizona University Press

Bowell, E., McMahon, J., Horne, K. et al., 1978, BAAS 10, 594

Burns, J.A., Safronov, V.S., 1973, MNRAS 165, 403

Cohen, M., Witteborn, F.C., Carbon, D.F. et al., 1996, AJ 112, 2274+

Cohen, M., Witteborn, F.C., Roush, T., Bregman, J.D., Wooden, D.H., 1998, AJ 115, 1671

Drummond, J., Eckart, A., Hege, E.K., 1988, Icarus 73, 1

Drummond, J.D., Hege, E.K., 1989, in R.P. Binzel, T. Gehrels and M.S. Matthews (eds.), Asteroids II; Proceedings of the Conference, Tucson, AZ, Mar. 8-11, 1988 (A90-27001 10-91), pp. 171-191, Arizona University Press

[18] Long-Wavelength Spectrometer
[19] Short-Wavelength Spectrometer
[20] Heinrich-Hertz-Telescope
[21] James Clerk Maxwell Telescope
[22] Stratospheric Observatory for Infrared Astronomy
[23] Far Infra-Red and Submillimetre Telescope, ESA
[24] Space Infrared Telescope Facility, NASA

Drummond, J.D., Hege, E.K., Cocke, W.J. et al., 1985, Icarus 61, 232
Duncan, W.D., Sandell, G., Robson, E.I., Ade, P.A.R., Griffin, M.J., 1990, MNRAS 243, 126
Dunham, D.W., Dunham, J.B., Binzel, R.P., 1990, AJ 99, 1636
Dunham, E., 1991, Occultation Newsletter 5, 93
Emerson, J.P., 1994, in T.P. Ray and S.V.W. Beckwith (eds.), Star Formation and Techniques in IR and mm-Wave Astronomy. Lecture Notes in Physics 431, pp. 125-156, Springer-Verlag
Erikson, A., 1998, Ph.D. thesis, Freie Universität, Berlin, Germany
Golay, M., 1974, Introduction to Astronomical Photometry, Vol. 41 of Astrophysics and Space Science Library, Reidel Dordrecht
Hammersley, P., de Muizon, M.J., Kessler, M.F. et al., 1998, A&A, in press
Hansen, O.L., 1977, Icarus 32, 458
Kessler, M.F., Steinz, J.A., Anderegg, M.E. et al., 1996, A&A 315, L27
Kreysa, E., 1990, in ESA, From Ground-Based to Space-Borne Sub-mm Astronomy (see N91-21986 13-89), pp. 265-270, ESA
Kristensen, L.K., 1984, Astronomische Nachrichten 305, 207
Lagerkvist, C.I., Magnusson, P., 1990, A&AS 86, 119
Lagerkvist, C.I., Magnusson, P., Williams, I.P. et al., 1992, A&AS 94, 43
Lagerros, J.S.V., 1996, A&A 310, 1011
Lagerros, J.S.V., 1997, A&A 325, 1226
Lagerros, J.S.V., 1998, A&A 332, 1123
Lebofsky, L.A., Spencer, J.R., 1989, in R.P. Binzel, T. Gehrels, and M.S. Matthews (eds.), Asteroids II, pp. 128-147, Arizona University Press
Lebofsky, L.A., Sykes, M.V., Tedesco, E.F. et al., 1986, Icarus 68, 239
Lemke, D., Klaas, U., Abolins, J. et al. 1996, A&A 315, L64
LeVan, P.D., Price, S.D., 1984, Icarus 57, 35
Lindal, G.F., 1992, AJ 103, 967
Magnusson, P., Barucci, M.A., Drummond, J.D., Lumme, K., Ostro, S.J., 1989, in R.P. Binzel, T. Gehrels, and M.S. Matthews (eds.), Asteroids II; Proceedings of the Conference, Tucson, AZ, Mar. 8-11, 1988 (A90-27001 10-91), pp. 67-97, Arizona University Press
Martin, R.N., Baars, J.W.M., 1990, in Instrumentation in astronomy VII; Proceedings of the Meeting, Tucson, AZ, Feb. 13-17, 1990 (A91-29601 11-35), pp. 503-514, SPIE
Matson, D.L., Tedesco, E.F., 1992, in IRAS Minor Planet Survey, PL-TR-92-2049, Hanscom Air Force Base, MA., pp. 5-12, Phillips Laboratory
McCarthy, D.W.J., Freeman, J.D., Drummond, J.D., 1994, Icarus 108, 285
Merline, W.J., Stern, S.A., Binzel, R.P. et al., 1996, AAS/Division of Planetary Sciences Meeting 28, 1025+
Michalowski, T., 1996, A&A 309, 970
Millis, R.L., Wasserman, L.H., Bowell, E. et al., 1981, AJ 86, 306
Millis, R.L., Wasserman, L.H., Franz, O.G. et al., 1987, Icarus 72, 507
Morrison, D., 1977, Icarus 31, 185
Müllert, T., 1997, Ph.D. thesis, Ruprecht-Karls-Universität, Heidelberg
Neugebauer, G., Habing, H.J., Van Duinen, R. et al., 1984, ApJL 278, L1
Piironen, J., Magnusson, P., Lagerkvist, C.I. et al. 1997, A&AS 121, 489
Redman, R.O., Feldman, P.A., Matthews, H.E., Halliday, I., Creutzberg, F., 1992, AJ 104, 405
Rieke, G.H., Lebofsky, M.J., Low, F.J., 1985, AJ 90, 900
Saint-Pe, O., Combes, M., Rigaut, F., 1993, Icarus 105, 271
Schertl, D., Grieger, F., Hofmann, K.H., 1995, Planet. Space Sci 43, 313
Simpson, J.P., Cuzzi, J.N., Erickson, E.F., Strecker, D.W., Tokunaga, A.T., 1981, Icarus 48, 230
Spencer, J.R., Lebofsky, L.A., Sykes, M.V., 1989, Icarus 78, 377
Stooke, P.J., 1997, http://europa.geog.uwo.ca/stooke_personalhomepage
Taylor, G.E., 1981, J. British Astron. Assoc. 92, 13
Tedeso, E.F. (ed.), 1992, IRAS Minor Plante Survey, PL-TR-92-2049, Hanscom Air Force Base, MA., Phillips Laboratory
Tedesco, E.F., Fowler, J.W., Chester, T.J., 1992, in IRAS Minor Planet Survey, PL-TR-92-2049, Hanscom Air Force Base, MA., pp. 127-148, Phillips Laboratory
Tedesco, E.F., Taylor, R.C., Drummond, J. et al., 1983, Icarus 54, 23
Tholen, D.J., 1984, Ph.D. thesis, Univ. of Arizona
Thomas, N., Fitzsimmons, A., Ip, W.-H., 1997, Planet. Space Sci. 45, 295
Tsvetkova, V.S., Dudinov, V.N., Pluzhnik, E.A., Shkuratov, I.G., Novikov, S.B., 1991, Icarus 92, 342
Wasserman, L.H., Millis, R.L., Franz, O.G. et al., 1979, AJ 84, 259
Zellner, B., Bowell, E., 1979, in A.H. Delsemme (ed.), Comets, Asteroids, Meteroites, pp. 185-197, The University of Tokio